

Narrow-angle scatter of reflectivity-suppressing nanostructured surfaces

David A. Gonzalez[Ⓞ],^{a,*} Jesus Meza-Galvan,^b David Sharp,^b
Karun Vijayraghavan,^b and Menelaos K. Poutous[Ⓞ]^a

^aUniversity of North Carolina at Charlotte, Department of Physics and Optical Science,
Charlotte, North Carolina, United States

^bNanohmics, Inc., Austin, Texas, United States

Abstract. Antireflective nanostructured surfaces (ARSS) enhance optical transmission through suppression of Fresnel reflection at boundaries between layered media. Previous studies show that random ARSS (rARSS) exhibit broadband enhancement and polarization insensitivity in transmission when applied to flat optical windows. Zinc selenide windows with rARSS treatment were fully characterized (transmittance, reflectance, and angular scatter) in the midwave and long-wave infrared range (2 to 12 μm). Four morphologically different, random nanoroughness, antireflective surfaces were tested at: normal incidence transmission, at 15 deg angle of incidence, and 15 deg to 45 deg angle of reflection. The angular reflectance distribution resembles a diffuse dipole radiator due to the finite elongated beam cross section at the incidence surface. Scattering diagrams with main and side lobes are presented. Partially integrated scatter values were obtained, allowing the comparison of random antireflective boundary performance to optically flat surfaces. Comparing axial transmission and specular reflection with the scattered performance, an accurate determination of the redistribution of the incident energy is obtained. Measurements of the rARSS feature topology were determined from autocorrelation of the scanning electron microscope images of the nanoroughened substrates, to assess the structured surfaces' feature scales. The results show differences in scattered intensity over the wavelength bands of interest, correlating with surface random feature populations. © The Authors. Published by SPIE under a Creative Commons Attribution 4.0 Unported License. Distribution or reproduction of this work in whole or in part requires full attribution of the original publication, including its DOI. [DOI: [10.1117/1.OE.59.10.103106](https://doi.org/10.1117/1.OE.59.10.103106)]

Keywords: nanostructured surfaces; Fresnel reflection; antireflection structured surface; random structures; infrared optical windows; bidirectional scatter distribution; narrow-angle scatter.

Paper 20201000 received Aug. 21, 2020; accepted for publication Oct. 15, 2020; published online Oct. 27, 2020.

1 Introduction

Fresnel reflection occurs when light is incident on boundaries separating dielectric regions with different optical refractive indices. Antireflective (AR) treatments, such as thin-film coatings, suppress reflections by destructive interference along the propagating directional axis. Recent studies have demonstrated that random antireflective structured surfaces (rARSS) can be used as an alternative to thin film coatings, reducing Fresnel reflections in the visible and the infrared (IR).¹⁻⁸ Broadband response, high transmission across wide ranges of angle of incidence (AOI), and polarization insensitivity have also been reported.^{9,10} In general, the AR effects correlate with the density and depth of the nanostructures, simulating an effective medium gradient-index boundary profile, which reduces Fresnel reflectivity.

Optical windows with antireflective treatments are characterized in transmission or reflection using spectrophotometers. Transmission enhancement is determined when the nanostructured surface results are compared to that from an unprocessed sample.⁶ Although transmission enhancement can be achieved by the suppression of specular Fresnel reflection, the inverse argument does not hold. In cases where surface-induced scatter is evident, the on-axis spectral reflection and transmission can be reduced simultaneously. In those cases, the sum of the detected

*Address all correspondence to David A. Gonzalez, dgonza23@uncc.edu

power along the wavevector axis is lower than the total incident power; or, if the measurements are normalized to one of the measured quantities and extrapolated, the sum of the reflected and transmitted powers results in more than the incident normalization (i.e., >100%). This is mainly due to the random surface nanoroughness transverse feature size distribution (lateral cross sections), which scatters light nonspecularly and distributes irradiance within solid angles much wider than optical quality polished substrates do.

Off-axis specular performance in optics is examined using the general fundamentals of optical scatter. Residual surface roughness, subsurface scatter from coatings, particulate scatter and bulk scatter due to index fluctuations all need to be considered when characterizing the transmissive or reflective performance of an optical component.¹¹ Scatter induced at an interface can potentially diminish image contrast or resolution, inhibiting the performance of imaging or signal processing systems. Understanding the causes of scatter and its effects on the performance of optical components is necessary to optimize imaging systems that use multiple optical surfaces. While scatter can be detrimental to the performance of an optical system, it can also be used to preferentially suppress physical properties of optical interfaces by selectively adding features to produce a controlled scattering effect.

Topological nanoscale features on surfaces are described using statistical distributions, which quantify their transverse-size population groupings (cross sections), their packing density, and their height values (or depth below the original surface level). It has been shown that random rough surfaces generally have Gaussian distributions of scaled features and can be approximately characterized by a surface root-mean-square roughness parameter.¹² When feature distributions have spatial frequencies near the incident radiation value, the roughness is considered bandlimited (or relevant) and it results in observable diffraction effects. Redistribution of light from the wavevector axial region into wider angles correlates with the relevant high-spatial frequencies approaching the order of the incident wavelength; conversely, midspatial frequencies are generally responsible for broadening the near-specular beam width in the far field.¹¹ Statistical surface profiles, therefore, give insight into the directional scatter of interfaces and vice versa.

Mid-wave infrared (MWIR) and long-wave infrared (LWIR) measurements of spectral transmittance $[T(\lambda)]$ and reflectance $[R(\lambda)]$ are collected using spectrophotometers with temporally incoherent and unpolarized light sources (e.g., globars). Such instruments have much larger apertures than the wavelengths in the IR band, resulting in poor spatial coherence in addition to their poor temporal coherence due to the thermal nature of their light-emission mechanisms. Because of low coherence, interference phenomena induced between surfaces of relatively thick ($>500\lambda$) transparent substrates are not prominent. Additionally, spectrophotometers normalize their measurements using a “background spectrum” or baseline, which is taken differently for each type of data set. In transmission, the background is collected as the irradiance through the system in the absence of the substrate to be tested. In reflection, the background irradiance of the system includes a reflective mirror, which is a single-surface optical component. Although this restriction is not significant for opaque substrates within the test bands, for transparent substrates there are multiple “front-to-back” reflections that contribute to the detected signal, and the normalization is not strictly comparable. Spectrophotometric intensity measurements cannot distinguish between single-surface reflections and overlapping reflections from the front and back surfaces of a transparent substrate, especially when the two surfaces are not identical. Therefore, at off-normal-incidence reflection conditions, the “top” and “bottom” irradiance reflections will overlap and the measured angular intensity distribution will be higher than the “top” single-surface response alone [Fig. 1(a)]. For nanoroughened substrates, the directional distribution of light from the front and back surfaces contribution will have additional scatter, which is different than that of an optically flat sample. Due to the finite size of the movable collection mirror, scattered light outside the directional collection cone (AOC) is not captured. The redistribution of light from the specular region is quantified by measuring wide-AOC intensities and comparing the angular distribution of light from a processed substrate to the optically flat (unprocessed) substrate [Fig. 1(b)].

During a reflection measurement, the incident beam is directed at the sample surface and reflected toward a collection mirror. The spectrophotometer used in this study is limited in motion along the counterclockwise directional sense. Depending on the optical system's

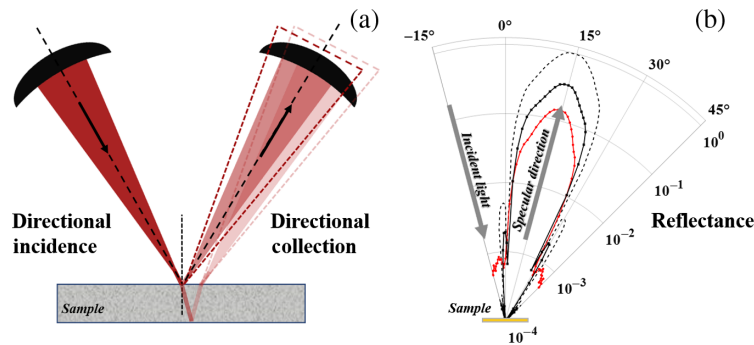


Fig. 1 (a) Configuration of reflection measurement of the spectrophotometer used in this study. Light is focused onto the transparent sample plane and the reflected cone of light (red shaded area) is collected by rotationally scanning the collection mirror. Nanoroughened substrates may scatter light outside of the directional cone of collection (dotted outlined area). (b) Angular intensity distribution is presented as a directional diagram from -15 deg to 45 deg AOC on a radial logarithmic normalized power scale. An aluminum mirror is used as a background (dashed line). Main lobe, side lobe, and wide-angle scatter ($> \pm 15$ deg from specular) of nanoroughened sample's intensity distribution (red circles) is quantitatively examined for changes in magnitude, width, and shape compared to the optically flat sample (black squares).

alignment, signature data associated with the background may exhibit biasing in one angular direction, causing an asymmetric pattern to form.¹¹

Transparent optical components are used exactly because of their transparency, and therefore, suppressing this secondary contribution during measurements does not provide a good comparison of overall component functionality. For a transparent substrate with a nanostructured AR surface, determination of the surface's bidirectional scatter (BDS) due to the scale of the random structures is desired. Since the instrument directly measures only specular spectral reflectance, including the background and double-reflection limitations mentioned above, one cannot assume that single-surface reflectance is to be completely determined by a single transmittance spectrum or the inverse. To determine BDS, both $R(\lambda)$ and $T(\lambda)$ have to be measured. The subtlety is to extract meaningful comparisons between optical single-surface reflectance, for components that have an AR nanostructured surface with respect to the original planar polished surface condition with the presence of the second (back) substrate surface contribution.

The purpose of this report is not to compare random surface-nanostructure fabrication methods and their relative effectiveness, nor to contrast AR performance of nanostructures compared to conventional thin-film coatings. We present complete sets of reflection, transmission, and near-specular angle scatter measurements due to the presence of randomly structured surfaces, realized using a controlled fabrication process.

2 Experimental Procedure and Results

Optical-quality ZnSe windows were used to fabricate and measure random antireflective nanostructure scatter effects in the bands of interest mentioned before. The 25.4-mm-diameter round substrates had an optical quality polish, with a measured 7-nm average roughness, 9-nm root mean square (rms) roughness, and a thickness of 3 mm. The random nanostructuring of the surfaces was achieved using the "thermodot" method described in detail elsewhere.¹³ For completeness, the method is outlined in brief below.

Figure 2 shows scanning electron-microscope (SEM) images of four, randomly nanostructured, zinc selenide surfaces (ZnSe:A–D), a common material used for IR optics. The optical substrates were coated with a thin, hard dielectric film (in this case AlN) at an empirically determined thickness, which is sufficient to mask the substrate from the reactive-ion plasma etching radicals for the duration of the fabrication etch process. A thin layer of metal (Ni) is deposited on top of the dielectric film, and it is rapidly annealed to form nanoscale islands on the dielectric surface. The density of the metallic islands is controlled by the rapid thermal annealing process

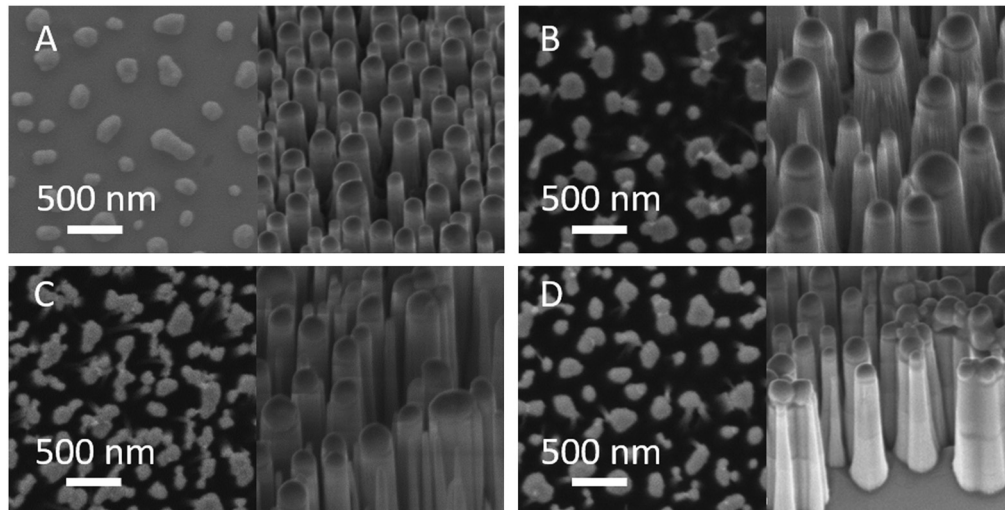


Fig. 2 For each of the four ZnSe-panels: top-down (left side) and 45 deg tilt view (right side) SEM images of nanostructured ZnSe pillars from the tested substrates.

schedule and the surface energy between the metal and the dielectric, whereas the island height is a function of the deposited metal-film thickness. In Fig. 2-ZnSe:A, a top-down SEM image of the thermodots on the dielectric surface is shown. The dots, controlled by the thermal process parameters, can vary in footprint shape and diameter—with an averaged-diameter population distribution that is statistically repeatable. The nanoisland statistical description (averaged diameter, proximity, and density) is measured using a numerical autocorrelation of the top-down SEM images. The transverse spatial frequency upper and lower limits are determined by this calculation, corresponding to nanoisland average cell size and diameter, respectively, which is then used to compute the average spacing dimension between the metal dots. Although the autocorrelation method is not as descriptive as granulometric histograms,⁹ comparative results within the set of measurements allow classification of the samples by feature scales.

The hard dielectric (AlN) is etched completely from the metal-vacant areas in a reactive-ion plasma (RIE), resulting in transfer of the random island metal-footprint patterns in the AlN layer. The random surface pattern is then etched through using a substrate-selective plasma, resulting in pillars with a “top-capped” profile (Fig. 2-ZnSe:A-right panel). The thermidot Ni masking caps were removed after the substrate etch step using a commercially available wet chemical Ni-etchant solution. The residual AlN caps remain on the original substrate pillars. The height of the pillars is controlled by the total etch time, whereas the chamber pressure and applied rf-power RIE parameters control the sidewalls of the pillars. The random-surface feature scale values for each of the four samples used in this study were measured and are listed in Table 1.

Table 1 Surface randomness averaged dimensions for ZnSe samples featured in Fig. 1.

Surface parameter (for islands/pillars)	ZnSe:A	ZnSe:B	ZnSe:C	ZnSe:D
Diameter (nm)	214	233	175	174
Cell size (nm)	487	457	360	368
Spacing (nm)	273	224	185	194
Height (nm)	653	1600	2500	1600
Density ratio (%)	44	51	49	47
Aspect ratio	3.05	6.87	14.29	9.20

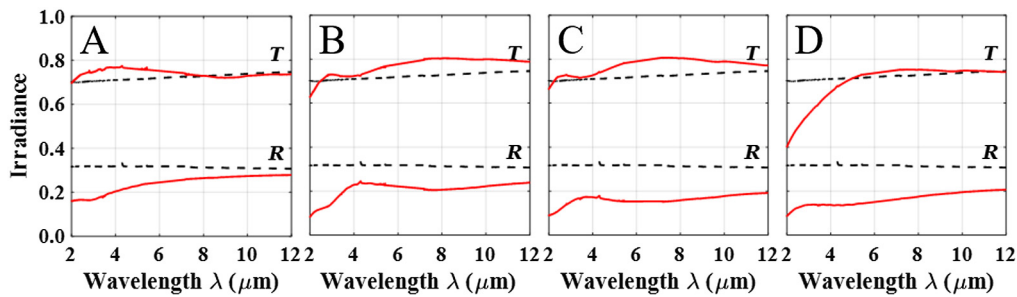


Fig. 3 Measured normal incidence (axial) transmission (T) and specular reflection at 15 deg (R), for the single-surface rARSS processed samples (red solid lines) and an optically flat ZnSe substrate (black dashed lines).

The pillar density ratio, calculated as the ratio of the average diameter to cell size, and their height-to-diameter aspect ratio, are comparative indicators of the random pattern density and effective depth. The pillar height is measured from the 45-deg-tilted, wide-field-of-view SEM images, with the appropriate geometrical corrections. For the representative sample group shown in this report, the pillar density varies from 44% (ZnSe:A) to 51% (ZnSe:B), and the aspect ratio from 3 (ZnSe:A) to 14 (ZnSe:C). Qualitatively, we can describe the samples tested as ranging from shallow and sparse (ZnSe:A) to deep and dense (ZnSe:C).

Spectral $T(\lambda)$ and $R(\lambda)$ were measured for all ZnSe substrates shown in Fig. 2. The measurements were collected using a spectrophotometer (Bruker, Vertex-V80), across the MWIR and LWIR spectrum (2 to 12 μm), at normal incidence for $T(\lambda)$ and at 15 deg AOI for $R(\lambda)$, sweeping AOC from 15 deg to 45 deg. For unpolarized and incoherent light, specular reflectivity is not appreciably changing for angles between normal incidence and the substrate's Brewster angle value. This allows a good approximation, pairing the 15-deg AOI $R(\lambda)$ data with the normal-incidence $T(\lambda)$ measurements. The results of the specular reflection and axial transmission are shown in Fig. 3.

Three of the four ZnSe nanostructured substrates, ZnSe:A, B, and C, have axial transmission enhancement within the wavebands measured, due to the presence of the rARSS on a single facet. At MWIR wavelengths (3 to 5 μm), summing the normalized axial transmission and reflection from the processed samples does not yield unity (100%) within our measurement's degree of uncertainty ($\pm 0.5\%$), suggesting there is an additional mechanism that is removing light from the axial light-propagation direction. Transmission is enhanced by 7% for sample A at MWIR wavelengths, whereas samples B and C have increased transmission (+10%) in the LWIR (8 to 12 μm). Sample D shows no improvement across the measured wavelength bands. Although the measured spectra of samples B and C are similar, it is noted that the surface features of the two samples shown in Fig. 2, and the surface randomness scale descriptors in Table 1, are morphologically distinct. The most noticeable difference between the two samples is their pillar aspect ratio, which is more than twice as large for sample ZnSe:C, whereas the pillar density ratio is more comparable between the two. The transverse-feature cell size is smaller for ZnSe:C compared to ZnSe:B, and almost identical to ZnSe:D. On the other hand, ZnSe:A and B have the same cell size and clearly different pillar aspect and density ratios.

Total integrated scatter (TIS) is a measure of all scattered intensity outside the region strictly defined by the light beam along the axial or specular direction. TIS can be useful for reducing large amounts of scattering data to a single comparative quantity, which defines the general scattering performance of optical interfaces. Due to the finite size of the spectrophotometer's collection mirror, the specular region is taken as the cone of collection spanned by the mirror, defining a limited integrated scatter region (Fig. 1). When testing transparent windows, surface scatter propagates in both the reflection and transmission directions; therefore, the spectrometer's detector mirror collects integrated scatter data in the transmission mode over the finite collection aperture as well. By combining the data of both the transmitted partial integrated scatter (contained in our normal incidence axial direction), as well as the integrated scatter cone of the specular reflection, BDS can be determined to further distinguish between the scattering induced by the various roughened surfaces.

As mentioned earlier, wide-angle scattered light escapes the spectrometer's cone-of-collection. To calculate the BDS, due to a single nanostructured surface on a transparent substrate, the unprocessed sample's double-sided (UDS) intensity measurements $T_{\text{UDS}}(\lambda)$ and $R_{\text{UDS}}(\lambda)$ are first summed to quantify the instrument's total measured irradiance reference. This value is used as a renormalization

$$T_{\text{UDS}}(\lambda) + R_{\text{UDS}}(\lambda) = I_U(\lambda) \cong 1. \quad (1)$$

In general, these quantities are normalized independently by the instrument and may not add to unity (100%), as their respective "baseline" normalizations are different: in the $R_{\text{UDS}}(\lambda)$ case there is a front surface metal mirror, whereas in the $T_{\text{UDS}}(\lambda)$ case it is the unobstructed incident light beam. We assumed that the unprocessed substrates, having a high-quality optical polish, have no appreciable scatter within the dynamic range of the spectrophotometer's detector. Following Eq. (1), the nanostructured surface sample's measurements $T_{\text{PDS}}(\lambda)$ and $R_{\text{PDS}}(\lambda)$ can be added to give

$$T_{\text{PDS}}(\lambda) + R_{\text{PDS}}(\lambda) + \Sigma_{\text{PSS}}(\lambda) = I_P(\lambda) + \Sigma_{\text{PSS}}(\lambda) = 1, \quad (2)$$

where $\Sigma_{\text{PSS}}(\lambda)$ is the noncaptured single-surface BDS and $I_P(\lambda)$ is the total irradiance measured by the instrument. Dividing Eq. (2) by Eq. (1), we proceed to calculate the net scattered irradiance ratio $\sigma_{\text{PSS}}(\lambda)$, which is normalized to the nonscattering, unprocessed substrate's total irradiance

$$\sigma_{\text{PSS}}(\lambda) = 1 - \left[\frac{I_P(\lambda)}{I_U(\lambda)} \right]. \quad (3)$$

Renormalization of the processed window reflection and transmission to the unprocessed sample values eliminates the unprocessed back-surface intensity contributions, common to all tested substrates, and produces a value for the radiative BDS, depending only on the presence of the processed single-sided surface. If the sum from Eq. (1) results to values near unity across the entire spectral range of measurements, then the single-surface scatter $\Sigma_{\text{PSS}}(\lambda)$ in Eq. (2) and the scattered irradiance ratio $\sigma_{\text{PSS}}(\lambda)$ from Eq. (3) are going to be within the instrument's measurement uncertainty, and we can consider them equal. Proceeding with this assumption and rearranging Eq. (2), we can relate the processed samples $R_{\text{PDS}}(\lambda)$ to the unprocessed sample double-sided intensity measurements $R_{\text{UDS}}(\lambda)$ by a wavelength-dependent scaling factor $f(\lambda)$

$$1 - \sigma_{\text{PSS}}(\lambda) - T_{\text{PDS}}(\lambda) \approx R_{\text{PDS}}(\lambda) = f(\lambda) \cdot R_{\text{UDS}}(\lambda). \quad (4)$$

In this sense, the processed scattering substrate is a "lossy" version of the double-sided polished substrate, with the losses attributed only to the single processed face. We note that $f(\lambda) < 1$, since the randomly nanostructured surface reflectance can only decrease along the specular direction as the scattered power will distribute over a solid angle of 2π steradians. Because all scatters are due to the single nanostructured surface, the same scaling factor could apply to the processed single-side reflectance $R_{\text{PSS}}(\lambda)$ relating it to the unprocessed single-side value $R_{\text{USS}}(\lambda)$

$$R_{\text{PSS}}(\lambda) \approx f(\lambda) \cdot R_{\text{USS}}(\lambda) = f(\lambda) \left\{ \frac{R_{\text{UDS}}(\lambda)}{[2 - R_{\text{UDS}}(\lambda)]} \right\}. \quad (5)$$

The last step in Eq. (5) is obtained by algebraic manipulation of the polished double-sided reflectance equation that relates the single side $T_{\text{USS}}(\lambda)$ and $R_{\text{USS}}(\lambda)$ to the double-sided quantity $R_{\text{UDS}}(\lambda)$.¹⁴

Using the preceding estimations, the total BDS: $\Sigma_{\text{PSS}}(\lambda)$, the single-side reflectance: $R_{\text{PSS}}(\lambda)$, and transmittance: $T_{\text{PSS}}(\lambda)$, for each ZnSe rARSS sample in Fig. 1 were calculated and shown in Fig. 4. As expected, the scatter is high for shorter wavelengths (MWIR) and decays as wavelengths increase (LWIR). Some qualitative comparisons are evident. The surface of sample A has fine and sparse nanoroughness inducing almost uniform low scatter across the wavebands.

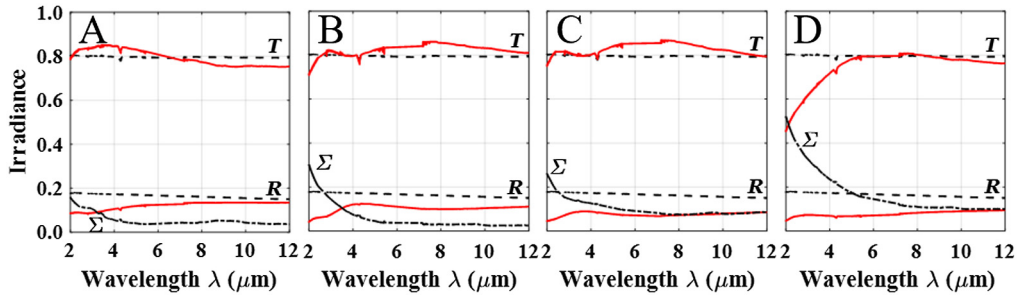


Fig. 4 Calculated BDS (Σ) (dash-dotted line), single-surface reflectance (R), and single-surface transmittance (T) for each single-surface processed ZnSe substrate (red solid line), and the optically flat ZnSe window (dashed line) in Fig. 1, using Fig. 3 measured spectra and Eqs. (3)–(5). Light scatter from the optically flat substrate was negligible over the wavelength band of interest.

Consequently, the transmittance of ZnSe:A in Fig. 3 shows a transmission enhancement result in the MWIR, and some scattering losses at the LWIR. In contrast, sample ZnSe:D, with larger and wider features, shows strong scattering in the MWIR, which affects its transmittance considerably.

Off-axis reflectance was measured as the collection mirror was swept from $\theta_c = 15$ deg to 45 deg, keeping AOI fixed at 15 deg. The variation in the collected radiance is due to the angular dependence of the reflected area-solid angle product $dA_s d\Omega_s$. Due to the elongation of the incident beam’s finite cross section in one direction $dA_s / \cos \theta_i$, the signature of the tool (single-surface mirror) appears to be similar to a diffuse dipole radiator. For transparent substrates, the double reflection will extend the apparent radiator length due to overlapping front-to-back reflected elliptical spots, accentuating the radiator’s characteristic shape.

Verification of the spectrophotometer set up alignment was conducted by taking measurements at 25 deg and 30 deg AOI, sweeping AOC (15 deg to 60 deg) to determine the symmetry of the tool’s signature intensity angular distribution. In those test cases, the clockwise and counterclockwise power distributions measured were approximately equivalent within the sensitivity of the instrument. After verification of the optical system limitations, the angular reflection data taken at 15 deg AOI, 15 deg to 45 deg AOC, was mirrored over the specular ray axis to produce a complete directional view of the scattered light distribution; however, we note that the data shown here consist only of counterclockwise-sense (increasing positive angle) reflectance measurement distributions.

Samples of the polar logarithmic-scale intensity distributions, at 4 and 10 μm wavelengths, are presented in Figs. 5 and 6. These figures show main- and side-lobe directional diagrams for each nanoroughened sample, the optically flat window, and the aluminum mirror. By examining the width (angular spread) and magnitude (reflection suppression) of the main and side lobes in the directional diagrams, we can make qualitative comparisons of the nanotextured surface performance compared to the optically flat sample. At an incident wavelength of 4 μm (Fig. 5),

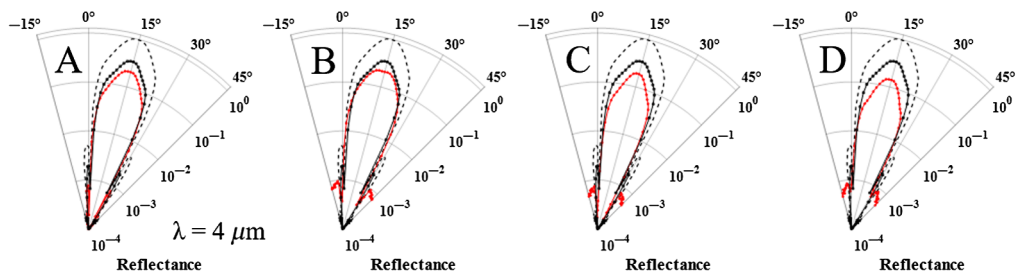


Fig. 5 Measured reflected directional intensity distributions at 4- μm wavelength, including scattered light outside of the directional cone ($+3 \text{ deg} < \theta_c < +27 \text{ deg}$). The processed surface (red circles) is compared to its unprocessed counterpart (black squares) and the mirror signature (dashed line).

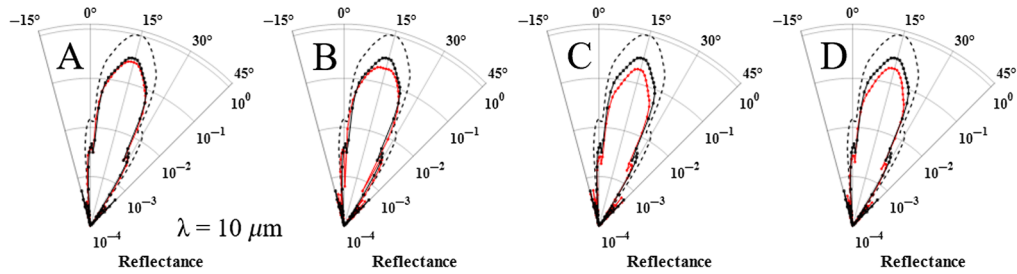


Fig. 6 Measured reflected directional intensity distributions at 10- μm wavelength, including scattered light outside of the directional cone ($0 \text{ deg} < \theta_c < +30 \text{ deg}$). The processed surface (red circles) is compared to its unprocessed counterpart (black squares) and the mirror signature (dashed line).

redirected light is observed at wide angles for samples B, C, and D, within $-15 \text{ deg} < \theta_c < +3 \text{ deg}$ and $+27 \text{ deg} < \theta_c < +45 \text{ deg}$, including the elimination of the side-lobe signature shape and increased wide-angle scatter, which is an order of magnitude higher than the optically flat sample at similar AOC. Additionally, samples B and C show a redistribution of light within the directional cone of collection ($+3 \text{ deg} < \theta_c < +27 \text{ deg}$), signified by the respective widening and narrowing of the main-lobe shape. Sample A shows reduction of main- and side-lobe magnitudes without significant redistribution of light from the specular region into the wide-angle region ($+3 \text{ deg} < \theta_c \text{ or } \theta_c > +27 \text{ deg}$) or change in signature shape compared to the unprocessed window. In the LWIR band (Fig. 6), the directional diagrams of all samples resemble the signature of the optically flat sample, with reduction in magnitude of the main lobe and side lobe due to suppression of the processed substrate's Fresnel specular reflectivity. Wide-angle scatter of all samples is on the order of the optically flat substrate scattered intensity values.

3 Analysis and Discussion

Polar representation of scattering data is useful to visualize the directionality of light within an optical system. Logarithmic-scale intensity distinguishes between the reflectivity of the main and side lobes of the directional diagrams, which can have four or more orders of magnitude difference. The angle of collection (θ_c) can be scaled in a semilogarithmic format, similar to conventional scattering formatting used by Harvey.¹¹ Using the parameter $\beta = \sin(\theta_c)$, scattering data can be compared over multiple AOI due to the shift invariance of radiometric radiance. The reflectance ratio presented here may not be considered radiance in a strict sense; however, plotting as a function of β allows for efficient examinations of the axial, narrow, and wide-angle scatter distributions compared to the polar representation, which can obfuscate wide-angle ($> \pm 15 \text{ deg}$ from specular) low-intensity data near the polar origin, such as in Figs. 5 and 6. We investigated the spectrum data using this representation. Selected scattering profiles at 4 μm (Fig. 7) and 10 μm wavelengths (Fig. 8) are presented below.

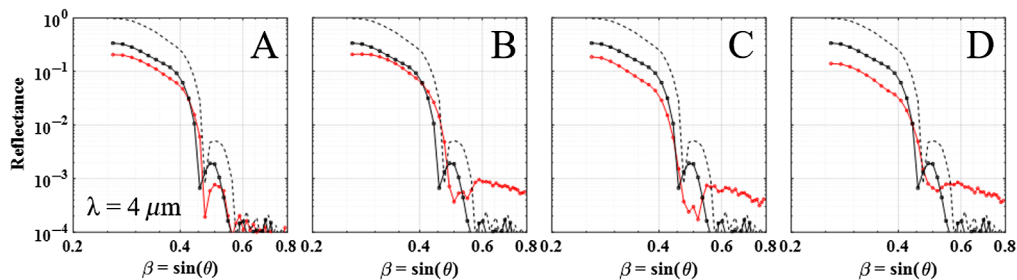


Fig. 7 Measured reflected angular intensity distribution at 4.0- μm wavelength, from the rARSS substrates (red circles), the unprocessed ZnSe window (black squares), and the reference mirror (dashed line), presented as logarithmic reflectance functions of parameter β .

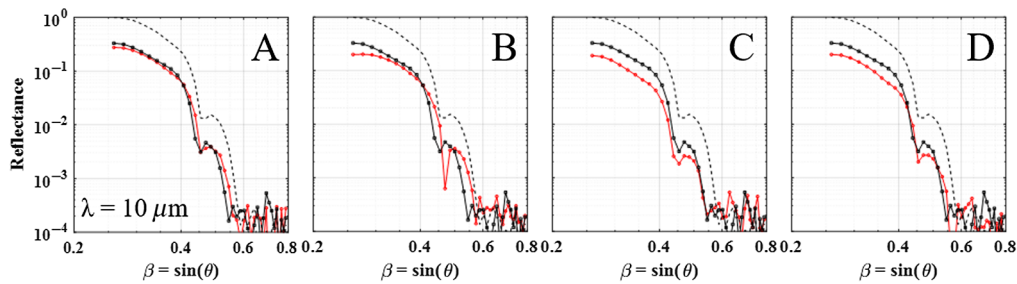


Fig. 8 Measured reflected angular intensity distribution at 10- μm wavelength, from the rARSS substrates (red circles), the unprocessed ZnSe window (black squares), and the reference mirror (dashed line) presented as logarithmic reflectance functions of parameter β .

Main and side lobes of the unprocessed sample measured scattering distribution are proportional to the measurement mirror performance (background), with a uniformly reduced magnitude due to the lower Fresnel reflectivity of ZnSe. Scaled conformity of the angular reflectance distribution signifies that scatter due to the presence of particulate contamination is minimal for the optically flat window. The mirror's and unprocessed sample's main lobe angular extent remains constant for $0.26 < \beta < 0.45$ ($15 \text{ deg} < \theta_c < 27 \text{ deg} \pm 0.5 \text{ deg}$) over the measured wavelength band, whereas the side-lobe intensity increases proportionally with wavelength, and its angular extent does not change appreciably ($7 \text{ deg} \pm 0.5 \text{ deg}$). Samples ZnSe:A, B, and D all exhibit broadening of the main lobe angular extent. The side lobes for samples B, C, and D are suppressed at the 4.0- μm wavelength, and the wide-angle scatter is an order of magnitude higher than the optically flat substrate. At the 10- μm wavelength, sample ZnSe:B shows broadening of the main lobe angular extent. Sample A performance matches the optically flat substrate in magnitude and shape, and samples B, C, and D have reduced main- and side-lobe values, while maintaining the general shape of the signature of the mirror. Global IR-sources generally emit as blackbodies; therefore, uncertainty in the spectrophotometer normalization occurs when the background and measured data approach three orders of magnitude difference at longer wavelengths and large angles of collection. This agrees with the elevated "noise" on our LWIR band measurements for $\beta > 0.55$ compared to the MWIR measurements.

Global spectral reflectance contour maps, as functions of AOC and wavelength, were assembled from all measurements to determine the performance of each sample with respect to the measured parameter set in a continuous parameter space (Fig. 9). Characteristics of the optically flat sample reflectance include: a near uniform spectral performance over the MWIR and LWIR with respect to wavelength. The flat sample's radiance map (Fig. 9-ZnSe:O) has a clear separation between main and side lobes at $\beta = 0.45$ in the MWIR and a consistent loss of contrast between the lobes as the wavelength increases into the LWIR. At wide angles ($\beta > 0.5$), the floor value of our reflectance measurements (10^{-4}) is distinguishable across the entire wavelength band, with minor measurement fluctuations due to the source instability in the LWIR and at large AOC.

Processed samples (ZnSe:A–D) are characterized by comparing their reflectance distribution contour gradients to that of the optically flat sample (ZnSe:O). The spectral radiance maps show noticeable differences in performance for each sample at shorter wavelengths (2.0 to 5.0 μm) for all AOCs. Sample ZnSe:A exhibits a side-lobe reduced magnitude while samples B, C, and D all have a homogenization of the scatter distribution outside of the main lobe ($\beta > 0.45$). Main lobes of all samples measured decrease as the angular extent widens and the $\beta = 0.45$ boundary diffuses. For samples B, C, and D, scatter at higher angles in the MWIR is an order of magnitude larger than samples O and A. Longer wavelength measurements (5.0 to 12 μm) of all samples resemble the optically flat sample with reduced magnitude values. Contrast between main and side lobes of processed samples diminishes for samples A, C, and D, whereas sample B has a clearly defined separation between lobes at longer wavelengths.

A qualitative discussion of reflectance trends for each sample is necessary due to the large parameter space within which the samples were measured. Generally, comparison of relative

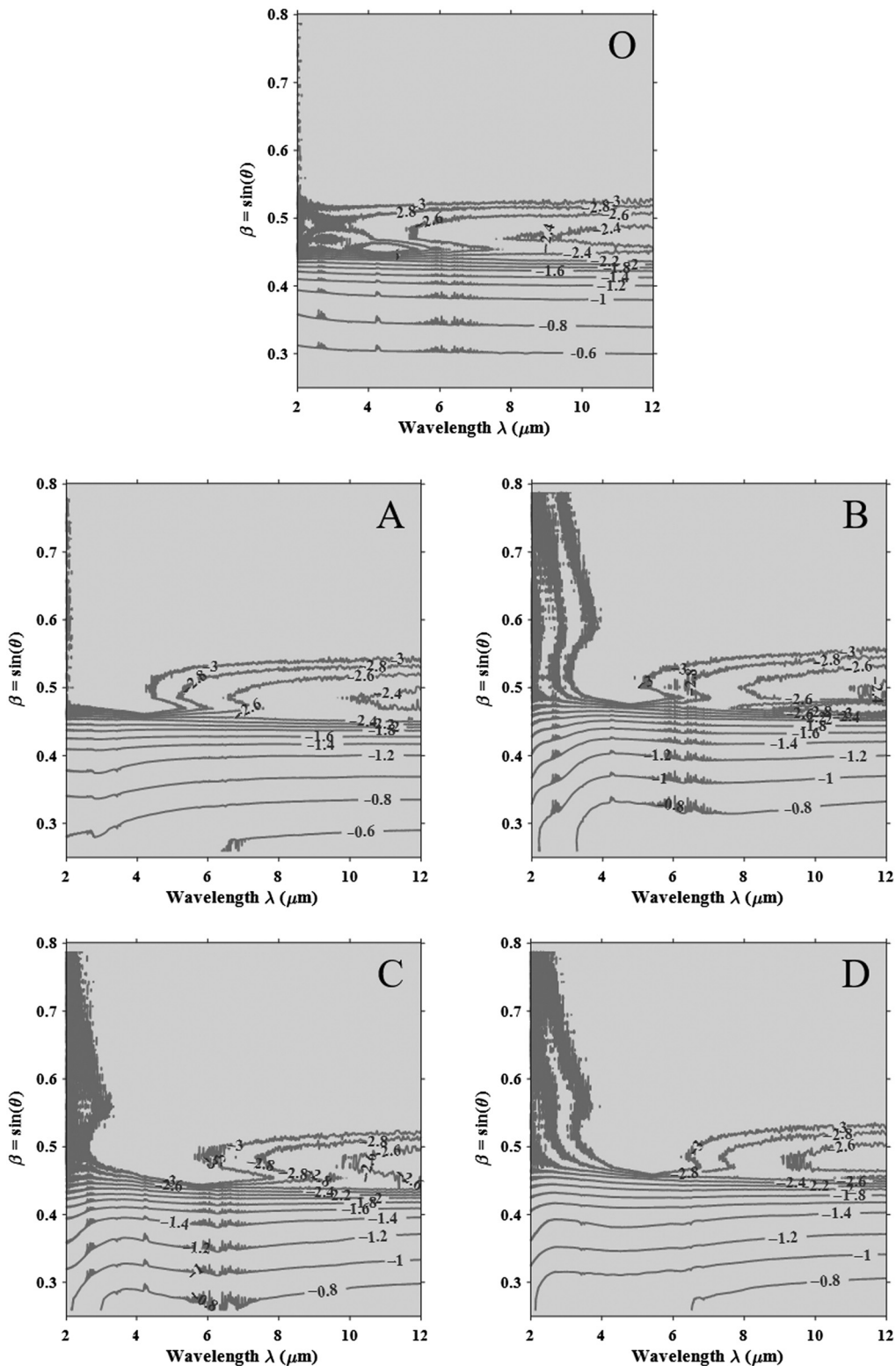


Fig. 9 Spectral reflectance contour maps for each ZnSe sample tested. The contour bands represent logarithmic reflectance values. ZnSe:O is the optically flat (unprocessed) window.

scattering trends between samples is important in the context of rationalizing the performance of an optical window due to the presence of roughness. In cases of randomly roughened window surfaces, modeling of the absolute scattering performance is difficult due to the limits of the statistical parameters with which we define the random surface. The conventionally used

rms-roughness measure is useful to qualify nanosurfaces due to the Gaussian distribution of depth features; however, extending the rms measure as a single-quality parameter can mask distinct surface scattering effects when the surface feature size distribution is on the order of the incident wavelength. The results shown in Fig. 9 show that a surface with shallow and sparse nanoroughness (ZnSe:A) has better MWIR antireflective performance than a shallow and dense surface (ZnSe:B), although in Fig. 3 the measured specular reflectance is lower for B compared to A. The AR-apparent reflective effect does not result in a transmission enhancement, just a redistribution of the incident energy in angular scatter reverse directions. Of note is that deep and sparse random nanostructures increase the wide-angle scatter considerably (ZnSe:D). Finally, for nanoroughness of the same density, comparing shallow (ZnSe:B) to deeper features (ZnSe:C), is not mitigating the MWIR wide-angle scatter losses. At the LWIR, deep nanoroughness is not enough to provide higher transmission enhancement. ZnSe:D and ZnSe:B have average feature depths of the order of 0.1λ and ZnSe:C is deeper at 0.25λ , yet B and C have very similar spectral responses strictly on-axis (Fig. 3). The fact that B and C have almost identical nanostructure densities, although their depths are dissimilar, seems to control the specular reflectance suppression. Given specular reflectivity and random surface depth measurements only, our results indicate that the axial transmission of random AR nanosurfaces cannot be accurately determined.

4 Conclusions

A method to quantify in detail the performance of randomly nanostructured AR surfaces on optical windows using single-sided-surface directional scatter reflectance and transmission measurements was presented, with the aim to remove normalization inconsistencies from measurements limited to nanostructured surface specular reflection alone. ZnSe windows with controlled AR-nanostructure variability were measured in specular reflection and axial transmission modes and normalized to optical-polished quality ZnSe surfaces. The nanostructured surfaces have cross-sectional features, which are, on average, dimensionally within one order of magnitude to the incident wavelength, a scale that requires measurement of directional scatter to determine the incident irradiance redistribution beyond the optical surfaces in both the forward and backward directions. The proposed method determines the surface-induced Fresnel reflectivity reduction, including the additional bidirectional scatter. The method requires axial transmission and specular reflection measurements of both the nanostructured surface and the optically flat equivalent material substrate, in order to remove the “backside” contribution of the transparent substrate and accurately determine the scatter due to the nanostructured surface alone.

Addition of surface nanoscale features on an optical surface provides suppression of Fresnel reflectivity in and at narrow-angle to the specular direction, and measurable off-axis redistribution of light into the wide-angle region. As the wavelength of light increases compared to the size of the surface features, the suppression of the directional radiation is less prominent, while the side lobes maintain comparable values to the optically flat substrate. This trend is evident when examining the magnitude of scattering at single wavelengths or angles of collection; however, this does not uniformly scale with light scatter from short to long wavelengths. We show these results, presenting reflectance measurements as a function of the directional parameter β and the incident wavelength for a selected set of sample surfaces. This analysis is only valid for single-side nanostructured substrates due to the backside contribution and the uncollected scatter in the axial transmission direction.

Suppression of the specular direction intensity does not imply an absolute enhancement of axial transmission through a nanostructured window; rather, an increase on the main- and side-lobe directional irradiance and angular spread is observed. MWIR scattering reflection distributions show an increase in specular scatter for all processed samples (Fig. 4). The directional angular irradiance distribution increases by 1 deg to 3 deg for all samples tested compared to the unprocessed sample, signifying a redistribution of the specular irradiance out of the ± 12 deg narrow angle of collection shown in Figs. 5 and 6. Additionally, samples ZnSe:B, C, and D have narrow-angle distributions replaced by uniform scatter, which resembles an inverse power law

function. In the LWIR, processed sample scattering distributions are closer to the values expected from an optically flat sample, with some reduction in the main- and side-lobe magnitudes. Wide-angle scatter ($> \pm 20$ deg from specular) is reduced to our measuring tool's noise level, signifying the feature sizes are too small to cause diffraction effects.

Measurements of the reflected angular intensity distribution of each processed substrate show the redistribution of light outside the specular direction, aligning with expectations based on the calculated BDS (Fig. 4). In the MWIR and LWIR, Fresnel reflectivity is shown to be suppressed in the specular region, because light is redistributed from that specular region. As the wavelength of incident light increases, the effects of scattering are less pronounced, yet measurable in the narrow axial direction regime.

Acknowledgments

The authors would like to acknowledge the financial support of Grant ARL-SBIR, No. W909MY-18-C-0018. The Bruker-V80 high-resolution spectrophotometer/reflectometer was funded by DURIP-ONR Grant No. N00014-14-1-0448.

References

1. Q. Yang et al., "Antireflection effects at nanostructured material interfaces and suppression of thin-film interference," *Nanotechnology* **24**, 235202 (2013).
2. Z. Lin et al., "Broad-band anti-reflective pore-like sub-wavelength surface nanostructures on sapphire for optical windows," *Nanotechnology* **29**, 055302 (2018).
3. S. Chattopadhyay et al., "Anti-reflecting and photonic nanostructures," *Mater. Sci. Eng.: R: Rep.* **69**, 1–35 (2010).
4. D. Hobbs, B. MacLeod, and J. Riccobono, "Update on the development of high performance antireflecting surface relief micro-structures," *Proc. SPIE* **6545**, 65450Y (2007).
5. D. Hobbs et al., "Laser damage resistant antireflection microstructures for midinfrared metal-ion doped ZnSe gain media," *Proc. SPIE* **8530**, 85300P (2012).
6. L. E. Busse et al., "Anti-reflective surface structures for spinel ceramics and fused silica windows, lenses and optical fibers," *Opt. Mat. Express* **4**(12), 2504–2515 (2014).
7. F. Gonzalez and M. Gordon, "Bio-inspired, sub-wavelength surface structures for ultra-broadband, omni-directional antireflection in the mid and far IR," *Opt. Express* **22**(11), 12808–12816 (2014).
8. D. Vandormael et al., "Anti-reflective sub-wavelength patterning of IR optics," *Proc. SPIE* **6395**, 63950L (2006).
9. A. Peltier et al., "Polarization insensitive performance of randomly structured antireflecting planar surfaces," *Opt. Eng.* **57**(3), 037109 (2018).
10. D. Gonzalez et al., "Optical scattering measurements of random anti-reflective nanostructured surfaces in the mid- and long-wave IR," *Proc. SPIE* **11289**, 112891Q (2020).
11. J. Harvey, *Understanding Surface Scatter Phenomena: A Linear Systems Formulation*, 1st ed., SPIE Press, Bellingham, Washington (2019).
12. J. Stover, *Optical Scattering: Measurement and Analysis*, 3rd ed., SPIE Press, Bellingham, Washington (2019).
13. B. Zollars, S. Savoy, and Q. Xue, "Antireflective structures for optics," US Patent Application Publication, US2015/0103396-A1 (2015).
14. O. Heavens, "Application of matrix method for evaluating reflectance and transmittance: a) The single film," in *Optical Properties of Thin Solid Films*, 2nd ed., pp. 76–78, Dover Publications, New York (1991).

David A. Gonzalez is a doctoral candidate in the Optical Science and Engineering Program at UNC Charlotte. His research efforts include fabrication of micro-optical elements, characterization of optical surface scatter, and laser damage testing of structured optical surfaces.

Menelaos K. Poutous received his doctorate degree from the School of Physics at the Georgia Institute of Technology in 1996. He is an associate professor in the Department of Physics and Optical Science at UNC Charlotte. He previously held a principal development engineer's position at Digital Optics Corporation, and before that, he was a physics lecturer at Emory University. His research interests are in spectroscopy, diffractive micro-optical elements, photolithographic microfabrication, and artificial optical surfaces.

Biographies of the other authors are not available.